Analysis of Fracture Orientation Data From Boreholes

STEPHEN J. MARTEL

*Department of Geology and Geophysics, University of Hawaii, 2525 Correa Road,
Honolulu, HI 96822*

Key Terms: *Fractures, Boreholes, Statistics, Rock Mechanics, Site Investigations*

ABSTRACT

Fracture orientation data from boreholes find widespread use in investigations of the subsurface. These data invariably are biased, with *in situ* fractures at low angles to a borehole being under-represented. Three statistical measures (mean spherical orientation, spherical variance, and moment of inertia), conventionally used to analyze axial data distributed on a sphere without corrections for borehole bias, are used here to analyze fracture pole orientations distributed on a hemisphere, with borehole bias being accounted for. By assuming a particular model for the *in situ* distribution of fractures, such as a uniform distribution, and then correcting for borehole bias, one can predict the distribution and statistics of fracture poles a borehole survey would yield. The model can then be modified based on the mismatch between observations and predictions. Geologic information on the kinematics and mechanics of fracturing can be incorporated into the model of the *in situ* distribution. An analysis of fracture orientation data from a complexly fractured granite at the Stripa mine in Sweden shows that this approach provides a useful and straightforward way to investigate fracture distributions in the subsurface. Moment of inertia diagrams and plots of cumulative distribution functions for fracture poles greatly augment equal area projections in analyzing fracture orientation data from boreholes.

INTRODUCTION

Fractures profoundly effect fluid flow, rock strength, and deformation over a broad range of spatial and temporal scales. Where fractures have a preferred alignment, they can impart a substantial anisotropy to a rock mass. Where fractures of varied orientation exist, they can form a well-connected network for fluid flow. As a result, fracture orientation data are collected for use in a wide variety of research investigations in geology, rock mechanics, geophysics, and hydrogeology (e.g., National Academy of Sciences, 1996). Fracture orientation data also are collected widely in industry for evaluating hydrocarbon reservoirs (e.g., Kulander et al., 1990) and the stability of rock slopes, foundations, and subsurface excavations (e.g., Goodman, 1976, 1980). Direct information on fracture orientations in the subsurface commonly is obtained with boreholes. However, as pointed out by Terzaghi (1965), boreholes introduce a pronounced observational bias into the data, with fractures at low angles to the borehole being under-represented. Properly accounting for borehole bias is essential where borehole fracture data are relied upon in evaluating the geology, mechanics, or hydraulics of a subsurface rock mass.

This manuscript presents a forward method for evaluating fracture orientation data obtained from boreholes. It illustrates how three well-known measures of directional data (the spherical mean direction, the spherical variance, and the moment of inertia) are affected by borehole bias. The manuscript also describes how these measures depend on the format in which the data are presented. The blend of directional data measures, correction for borehole bias, and treatment of hemispherical data is new and complements the work of Terzaghi (1965) and Priest (1985) on borehole bias.

The manuscript begins by reviewing the formats for describing fracture orientations. The observational bias introduced by boreholes is described next. An overview of a few simple distributions of biased and unbiased orientation data follows, along with an examination of the associated statistics. The forward modeling approach is then applied to data from complexly fractured granite at the Stripa mine in Sweden. This example shows how geologic data can be used to construct a testable model for the *in situ* distribution of fractures. Most of the mathematical presentation is confined to appendices to preserve readability, but particularly important concepts are treated in the body of the manuscript.

FORMATS FOR FRACTURE ORIENTATION DATA

The orientation of a fracture commonly is described in terms of the orientation of a vector, or a line, that is normal to the fracture and that passes through the center of a (hemi)sphere (Figure 1). A vector intersects a hemisphere in one point, whereas a line intersects a sphere
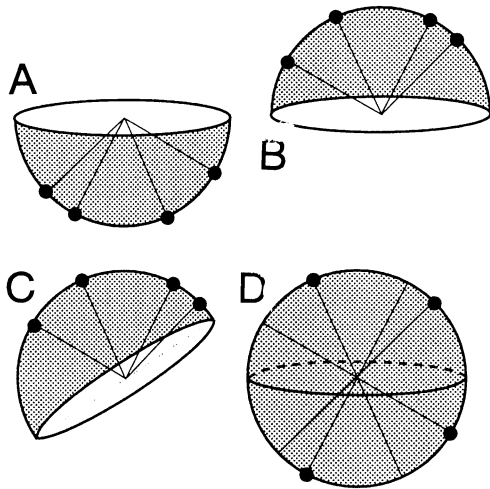
Figure 1. Distributions of fracture poles: A) lower hemispherical distribution; B) upper hemispherical distribution; C) distribution on a hemisphere with a non-horizontal projection plane; D) spherical distribution.

in two. In structural geology, orientation data are conventionally displayed using projections of a lower hemisphere with a horizontal diametrical plane (Hobbs et al., 1976; Goodman, 1976; Priest, 1985; and Fisher et al., 1987). In a spherical distribution (Fisher et al., 1987), both the upper and lower hemispheres are involved. Hemispherical projections with inclined diametrical planes are useful in analyzing borehole data if the normal to the inclined plane parallels the borehole axis.

As noted by Fisher and others (1987) lines are undirected axes and must be treated differently than vectors, which have directions. Axial data plot on both hemispheres in a spherical distribution, whereas a single vector plots on just one hemisphere. Treatment of axial data (e.g., Watson, 1965, 1966; Fisher et al., 1987) have focused on distributions of poles on a sphere rather than a hemisphere. A hemispherical format, however, has an advantage over a spherical format in describing fracture pole orientations: a single hemisphere allows no redundant information, unlike the two hemispheres that form a sphere. Furthermore, as is shown below, certain statistics of the two distributions differ. These statistics can be interpreted more readily for the hemispherical distribution.

The orientation of a fracture pole is described in a variety of ways; a few are used here. One is by its trend α and plunge η (Figure 2A). Alternatively, the pole can be described by its co-plunge γ, the angle of the pole relative to a vertical axis. The angles η and γ range between $0°$ and $90°$. The terms α and γ here correspond to ϕ and θ, respectively, of Fisher and others (1987). A second method is by direction cosines. The direction cosines $<u, v, w>$ are given here in terms of a reference frame where the x-, y-, and z-axes point north, east, and down, respectively (Figure 2A):

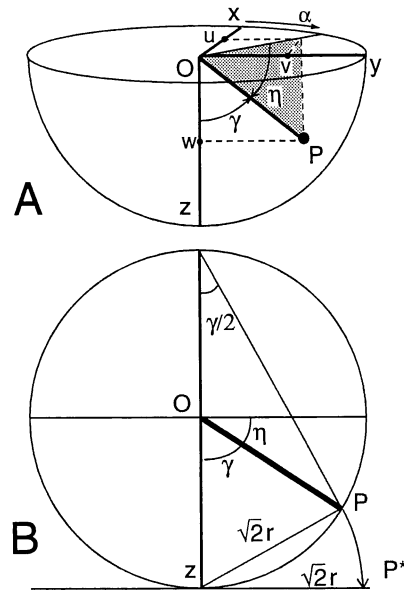$$u = \cos\alpha \, \sin\gamma \qquad \text{Eq. 1-1}$$

Figure 2. A) Reference frame for spherical coordinates, and B) the corresponding equal area projection in cross section. The sphere and hemisphere have a unit radius.

$$v = \sin\alpha \, \sin\gamma \qquad \text{Eq. 1-2}$$
$$w = \cos\gamma \qquad \text{Eq. 1-3}$$

The direction cosines of an upper hemisphere pole have the opposite sign of those for the corresponding lower hemisphere pole. For a lower hemisphere projection, the direction cosine w of each data point must have the same sign. The trend and co-plunge are readily found from the direction cosines:

$$\alpha = \tan^{-1}\left(v / u\right) + \frac{\pi}{2} \, \text{sgn}(u) - \frac{\pi}{2} \qquad \text{Eq. 1-4}$$

$$\gamma = \cos^{-1} w \qquad \text{Eq. 1-5}$$

The right side of Equation 1-4 represents the atan2 function present in several software packages (e.g., The MathWorks, 1992) and allows α to range from $-\pi$ to π. A third method (Figure 2B) is by equal area projection (Hobbs et al., 1976; Priest, 1985). The radial coordinate r of a fracture pole in this projection is $r = \sqrt{2} \sin\left(\gamma/2\right)$, and the angular coordinate is the trend α. The density of poles in an equal area projection faithfully reflects the pole density on the surface of a lower hemisphere.

Fracture orientation data from a borehole usually are collected relative to the orientation of a borehole (e.g., Goodman, 1976; Priest, 1985) before being translated to a geographic reference frame. These data are referred to as apparent orientation data. In one convenient borehole-based reference frame, the z*-axis parallels the borehole axis, the x*-axis lies in a vertical plane that

contains the borehole axis, and the y*-axis is horizontal (Figure 3A). Two angles describe the fracture orientation relative to the borehole. The angle γ^*, the apparent co-plunge, is the acute angle between a fracture normal and the down-hole direction of the borehole. The angle α^*, the apparent trend of the fracture pole, is measured around the hole circumference (Figure 3B). These two angles can be determined directly either from drill core samples or from the trace of a fracture on a borehole wall (Figure 3C). For an inclined borehole, α^* is the angle between a reference line parallel to, and on top of, the borehole (i.e., the "top line" of Figure 3) and the uphole end of the major axis of the ellipse formed by the intersection of the fracture and the borehole. The direction cosines in the borehole-based reference frame are $<u^*, v^*, w^*>$. The conversion of the apparent orientation data to an absolute reference frame is done readily using a rotation matrix aij (Gellert et al., 1977):

$$\begin{bmatrix} u \\ v \\ w \end{bmatrix} = \begin{bmatrix} a_{xx^*} & a_{xy^*} & a_{xz^*} \\ a_{yx^*} & a_{yy^*} & a_{yz^*} \\ a_{zx^*} & a_{zy^*} & a_{zz^*} \end{bmatrix} \begin{bmatrix} u^* \\ v^* \\ w^* \end{bmatrix} \qquad \text{Eq. 2}$$

where, for example, a_{xy^*} is the cosine between the x-axis in the absolute reference frame and the y*-axis in the borehole-based reference frame.

BOREHOLE BIAS

The probability of encountering natural fractures of a specified orientation with a borehole depends on factors such as: a) the abundance of fractures in the region sampled, b) the orientation of the fractures with respect to the borehole, c) the size of the fractures, d) the positions of fractures relative to the position of the borehole, e)

the length of the borehole, and f) the diameter of the borehole. The first two factors are the focus here, and fracture shape, in-plane dimensions, and spatial distribution are considered to be uniform.

Terzaghi (1965) presented the first paper in the English literature to focus on the effect of borehole bias on fracture orientation data. Her paper laid the foundation for subsequent work by Priest (1985) as well as the study here. Terzaghi noted that the distance between fractures of a given set along the length of a borehole depends on the orientation of the borehole relative to the fractures. For a set of extensive fractures with a uniform spacing, d, the number of fractures, N, intersected over a interval of length, L, along a borehole is (Terzaghi, 1965):

$$N = (L \sin\Psi)/d \qquad \text{Eq. 3-1}$$

where Ψ is the acute angle between the fractures and the borehole axis (Figure 4). For a vertical borehole, Ψ equals the plunge of the fracture pole, η (Figure 2). Equation 3-1 applies rigorously only if two conditions apply: a) fractures do not intersect the ends of the interval, and b) both ends of the interval are the same distance from the next fracture in the fracture set (i.e., L must be an integer multiple of $[\sin\Psi]/a$). If the first condition is not met, then N should be replaced by $N-1$. If the second condition is not met, then $[L\sin\Psi]/a$ will not be an integer. The second condition generally is not met, and the interval must intersect a large number of fractures for Equation 3-1 to yield a good approximation.

Using the angle γ^* instead of Ψ, Equation 3-1 can be expressed in a more general form useful for boreholes of arbitrary inclination:
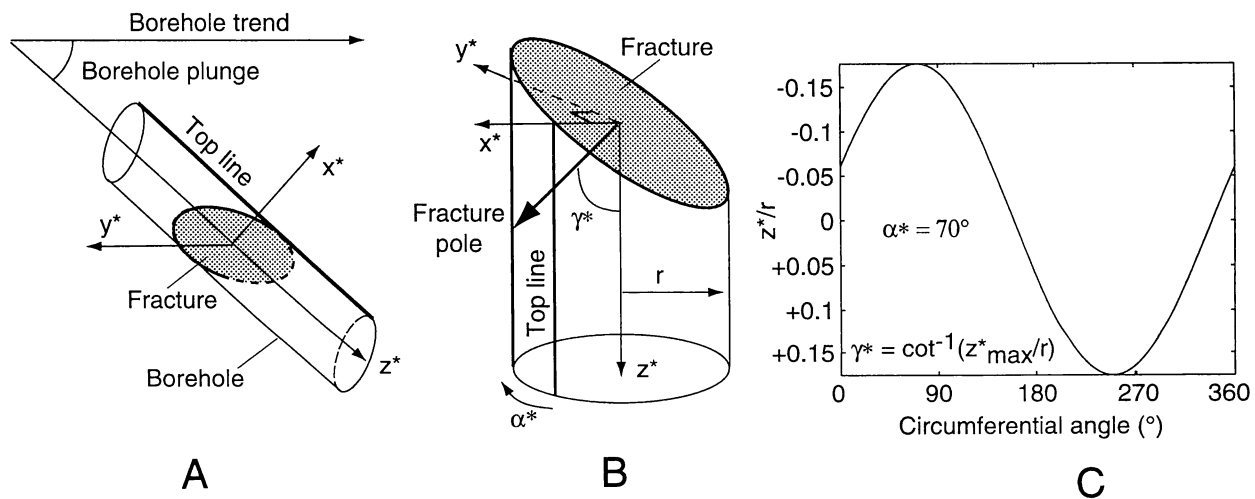
$$N = (L \cos\gamma^*)/d \qquad \text{Eq. 3-2}$$

Figure 3. Representations of a fracture intersecting a borehole: A) borehole-based reference frame; B) apparent trend (α^*) and apparent co-plunge (γ^*). Trace of a fracture on a downhole log.
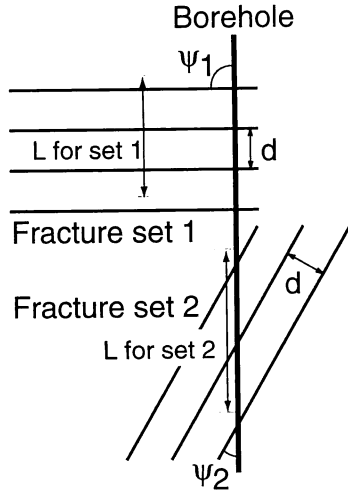
Figure 4. Diagram showing how the number of fractures intersected by a given length of borehole (*L*) varies with the angle ψ between the fractures and the borehole.

The term $\cos\gamma^*$ serves as a relative probability and ranges from zero to one. Figure 4 shows that the relative probability of intersecting a fracture where $\Psi = 90°$ ($\gamma^* = 0°$) is twice that where $\Psi = 30°$ ($\gamma^* = 60°$). A uniform change in the spacing between fractures or in their size changes the absolute probability of an intersection but not the relative probability $\cos\gamma^*$.

Terzaghi described a simple inverse technique to mitigate against this observational bias. She suggested that the fractures be divided into groups of essentially the same orientation (approximately the same strike and same dip) and the number of fractures in a given group *N* be replaced by *N**, where $N^* = N/\sin\Psi$. This, she contended, should yield a more representative picture of the *in situ* distribution of fracture orientations. Some care must be exercised, however, in defining the number and size of groups of fractures with essentially the same orientation, and *N** generally will not be a whole number. Also, Terzaghi cautioned against blind application of her inverse method for fractures nearly parallel to a borehole. A single such fracture might represent either a lone fracture that was sampled just by chance, or a member of a large set that was poorly sampled just because of its orientation. The effect of a lone fracture can affect *N** disproportionately, because the correction factor $1/\sin\Psi$ is large if Ψ is small. In light of these difficulties, Terzaghi considered fractures oriented at less than 20°–30° to a borehole to lie in a blind zone where fracture data would be difficult to interpret.

Forward modeling methods can overcome some of the difficulties with Terzaghi's inverse procedures. The methods are aided by some powerful yet simple statistical treatments not used by Terzaghi. Some of the more straightforward techniques are applied in the forward model here. An understanding of the kinematics and mechanics of fractures formation also can help in the

forward analysis as is shown in the examination of fractures at Stripa, Sweden.

TYPES OF DISTRIBUTIONS

This section focuses on two types of fracture pole distributions on a hemisphere: a) the uniform distribution, and b) the uniform distribution affected by borehole bias. A clear understanding of these distributions is essential to understand the remainder of this paper. Neither one, for example, is obtained by selecting pole trends and pole plunges at random. Both continuous and discrete approximations to these distributions are discussed.

These distributions are described using probability densities and cumulative distribution functions. These functions usually are represented in terms of a single variable, but they are introduced here in terms of two variables. The probability density (ρ) is a weighting function and refers here to the abundance of data (e.g., poles) per unit area of a projection surface. The cumulative distribution function (*cdf*) describes the proportion of data with values less than or equal to some specified value. Here the *cdf* represents the proportion of the data on some portion of the total projection area, *A*. The functions ρ and *cdf* are related as follows:

$$\int \rho \, dA = cdf \qquad \text{Eq. 4-1}$$

Evaluated over the entire area of the projection surface, the *cdf* equals one:

$$\int_A \rho \, dA = 1 \qquad \text{Eq. 4-2}$$

For a spherical or hemispherical surface, the incremental area *dA* depends on the variables α^*, the apparent trend, and γ^*, the apparent co-plunge (see Appendix A):

$$dA = \sin\gamma^* d\alpha^* d\gamma^* \qquad \text{Eq. 5}$$

Substituting Equation 5 into Equation 4-1 yields the *cdf* as:

$$\int_{\gamma^* = 0}^{\gamma^*} \int_{\alpha^* = 0}^{\alpha^* = 2\pi} \rho \, (\sin\gamma^*) \, d\alpha^* d\gamma^* = cdf \qquad \text{Eq. 6-1}$$

Substituting Equation 5 into Equation 4-2 yields

$$\int_{\gamma^* = 0}^{\gamma^* = \pi/2} \int_{\alpha^* = 0}^{\alpha^* = 2\pi} \rho \, (\sin\gamma^*) \, d\alpha^* d\gamma^* = 1 \qquad \text{Eq. 6-2}$$

The distributions considered here are axisymmetric about the $\gamma^* = 0$ axis, and so ρ is a function only of α^*. Equation 6-1 thus reduces to:

$$\int_{\gamma^* = 0}^{\gamma^*} 2\pi\rho \, (\sin\gamma^*) \, d\gamma^* = cdf \qquad\qquad \text{Eq. 6-3}$$

Equation 6-2 is solved for ρ, and then Equation 6-3 is solved for the *cdf* (Appendix B). For the distributions considered here, these functions are plotted in Figure 5.

The Uniform Distribution

For a uniform distribution, fractures poles have a uniform probability density on a sphere, hemisphere, or equal area diagram (Figure 6A). This distribution is simple and a useful standard for comparison. For a continuous uniform distribution of poles, ρ is a constant. For a hemisphere of unit radius, Equation 4-2 shows that ρ equals the reciprocal of the area of the hemisphere, so $\rho = 1/(2\pi)$. For a spherical distribution (Fisher et al., 1987), $\rho = 1/(4\pi)$.

A discrete approximation to a continuous distribution provides a useful comparison to real data. To obtain a set of discrete points that approximate a uniform orientation distribution on a lower hemisphere, three numbers are selected independently and at random: $-1 \le x \le 1$, $-1 \le y \le 1$, and $0 \le z \le 1$. This gives the x, y, and z coordinates of a point in the lower half of a cube with an edge half-length of one. Let d be the distance from the point to the origin. Points for which $d \le 1$ lie inside or on a unit hemisphere; they form set A. Points for which $1 < d \le 3^{1/2}$ lie outside the unit hemisphere and inside the half-cube; they form set B. Points of set B are concentrated in the lower corners of the half-cube. Both sets of points fill space uniformly. Dividing the coordinates of a point by its radial distance d essentially projects the point onto the hemisphere. The projection of set A, the uniform distribution within the hemisphere, yields a uniform distribution on the hemisphere. In contrast, the projection of the corner points of set B yields a non-uniform distribution on the hemisphere: the projected points cluster in the NE, NW, SW and SE quadrants of the hemisphere at a plunge of $\cos^{-1}[(1/3)^{1/2}]$, or about 35°. For this reason, only the points of set A are used: if $d > 1$, then the point is rejected.
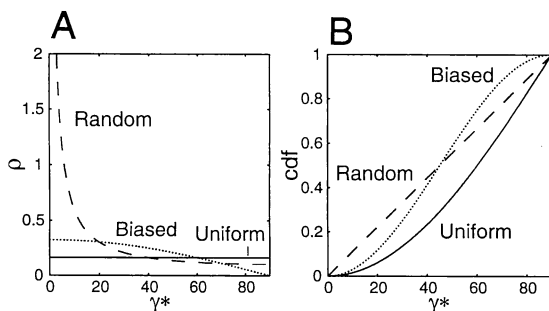

Figure 5. Diagrams of the theoretical distributions of (A) probability density ρ and (B) cumulative distribution function (cdf) for poles on a hemisphere. Solid curves are for a uniform distribution. Dotted curves are for a biased uniform distribution. Dashed curves are for poles defined by trends and plunges selected at random.

If $d \le 1$, each coordinate of the point is divided by d; this effectively projects the point onto a unit hemisphere. The new coordinate set represents the endpoint of a pole that uniquely specifies the orientation of a fracture. The apparent trend α^* and co-plunge γ^* of the fracture are found using Equations 1-4 and 1-5. The process is repeated as many times as desired to produce an approximately uniform coverage of points on a lower hemisphere (Figure 6A).

An alternative method (Haneberg, 1999, written communication) for generating a uniform distribution of pole orientations utilizes concepts of the equal area projection. Consider a circle of unit area and a smaller concentric circle inside it. The larger circle represents the primitive circle of an equal area projection. The ratio, m, of the areas of the circles equals the square of the radius of the small circle. Therefore, the square root of a number m chosen at random from a uniform distribution between zero and one yields the radius, r, of a circle that contains the proportion of points in a uniform density distribution equal to m (see Equation E-13). For example, if $m = 0.25$, then the probability is 25 percent of a point plotting within a distance of $r = 0.5$ from the center of a unit primitive circle. Combining values of m and r with α^* values chosen at random from a uniform distribution between 0° and 360° yield the co-plunge γ^* and trend of poles in a uniform distribution, with $\gamma^* = 2\sin^{-1}(r/\sqrt{2})$.

A discrete approximation to a uniform distribution is different from the one obtained by randomly selecting fracture pole trends between 0° and 360° and randomly selecting pole plunges between 0° and 90° (Figure 6B). Such a process yields an over-abundance of steeply plunging poles, as the cluster of poles near the center of Figure 6B reveals. For this distribution $\rho = 1/(\pi^2 \sin\gamma^*)$, as shown in Appendix B. Certain statistics of this distribution are similar to the one produced by sampling a uniform distribution with a borehole.

The Biased Uniform Distribution

A biased uniform distribution of fracture poles is produced by adjusting the density to account for the effect of borehole bias. As discussed above, the relative probability for this distribution is $\cos\gamma^*$. The probability density ρ for a continuous biased uniform distribution over a unit hemisphere is $\cos\gamma^*/\pi$ (see Appendix B).

To produce a discrete approximation to a biased uniform distribution, a sample is drawn from a uniform distribution, as described above, and a series of numbers N_i is obtained by sampling at random between zero and one. The ith fracture is considered as being intersected by a borehole if $N_i \le \cos\gamma^*_i$. This process is repeated to produce the desired number of samples. In the resulting biased distribution, fractures nearly perpendicular to the borehole are over-represented (Figure 6C) compared to
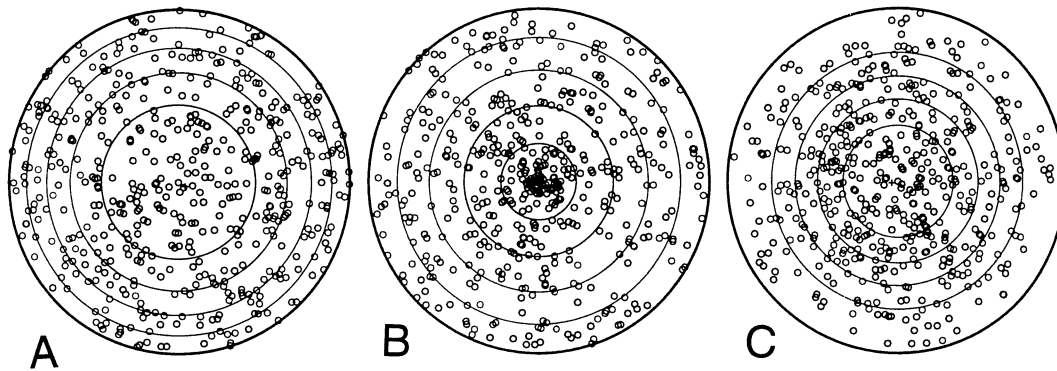
Figure 6. Equal area plots of 500 poles taken from A) a uniform orientation distribution, B) by combining randomly selecting pole trends between 0° and 360° and pole plunges between 0° and 90°, and C) for a uniform distribution affected by borehole bias. The concentric circles divide the plots into bins where equal numbers of poles are expected.

the uniform *in situ* distribution (Figure 6A). The clustering of poles in Figure 6C mimics that of Figure 6B. Sub-horizontal fractures are over-represented if the hole is vertical (Figure 6C); steeply-dipping fractures are over-represented if a hole is horizontal (Figure 7A). For inclined holes the poles have skewed distributions on equal area plots (Figures 7B and 7C).

Figure 7 illustrates four key points. First, clustering of fracture poles about the orientation of the borehole is a sign of borehole bias. Second, the magnitude of the borehole bias effect can be so pronounced that a cursory review of fracture orientation data obtained from a borehole could lead to a grossly incorrect estimate of the *in situ* fracture orientation distribution. Third, a given *in situ* distribution of fractures can yield markedly different absolute orientation distributions if investigated by boreholes of different orientation. Fourth, the axisymmetric nature of a uniform *in situ* distribution is most clearly represented where the orientation of the borehole is at the center of the equal area plot (Figure 6C). This last point indicates that plots of apparent orientation data can be useful in visually evaluating the effect of borehole bias (see also Appendix E).

ANALYSES OF DIRECTIONAL DATA DISTRIBUTIONS

Directional data distribution are analyzed in the geological literature (e.g., Scheidegger, 1965; Woodcock, 1977; and Fisher et al., 1987), but have not been investigated in the context of borehole bias. Three of the most common measures of directional data are discussed here in that context: spherical mean direction, spherical variance, and the principal moments of inertia. This section also contrasts these measures for data collected in hemispherical and spherical formats.

Spherical Mean Direction and the Spherical Variance

Two useful measures of fracture orientation data are the spherical mean direction and the spherical mean variance (Mardia, 1972; Fisher et al., 1987). They are calculated here by representing each fracture pole with a single vector of unit length. The vector length could be scaled to the area of a fracture, however, if the area were known. The spherical mean direction of a set of n vectors representing fracture poles is simply the
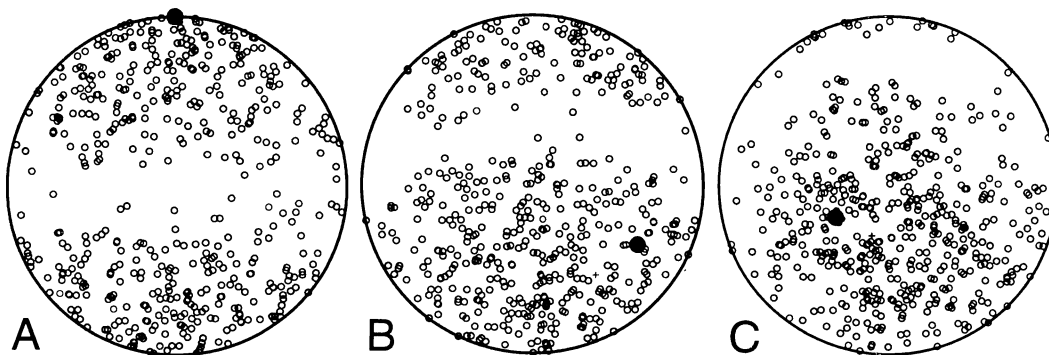

Figure 7. Equal area plots of poles to fractures formed by probabilistically sampling from a uniform orientation distribution to account for borehole bias. Borehole orientations are shown by heavy dots. In each case the fracture poles cluster around the orientation of the hole. A) Horizontal hole; B) hole trends 120°, and plunges 30°; C) hole trends 240°, and plunges 60°.

direction of the resultant vector R formed by summing all n unit vectors. The spherical variance S^* ($0 \leq S^* \leq 1$) is defined as $1 - (|R|/n)$, where $|R|$ is the length of the resultant. The quotient $R^* = |R|/n$ is the mean resultant length (Fisher et al., 1987). One would expect that values of S^* near zero should indicate a low degree of scatter in orientations.

Values for R^* and S^* for five axisymmetric pole distributions are presented in Table 1, with the supporting calculations in Appendix C. The examples involve: a) an even number of vertical poles, b) a biased uniform distribution, c) poles with trends and plunges chosen at random, d) a uniform distribution of many poles, and e) horizontal poles with a uniform distribution of pole trends. All of these cases are axisymmetric. In the spherical distributions, half the poles lie on an upper hemisphere and the other half on the lower. In each case involving a spherical distribution, $R^*_s = 0$ and $S^*_s = 1$. The first case shows that a high spherical variance, which seemingly should imply a large degree of scatter in the data, can reflect no scatter at all. In contrast, the normalized resultant length R^*_h, and variance S^*_h for the lower hemisphere distributions clearly are more indicative of variations in the data (see Table 1). These examples demonstrate advantages of a hemispherical format over a spherical format in examining fracture pole distributions.

For fracture orientation data obtained from nonvertical boreholes, meaningful hemispherical values of S^*_h and R^*_h are obtained readily using orientations of the fracture poles relative to the borehole (i.e., the "apparent" orientations of fracture poles). The values are meaningful because the z^* values for the poles pole have the same signs. If fracture pole orientations in a geographic reference frame are used directly to find S^*_h and R^*_h, then the direction cosines for each fracture pole first must be corrected by multiplying them by the sign of the cosine of the angle between the borehole and the fracture pole (i.e., the sign of the dot product between a vector parallel to the borehole and the fracture pole). Otherwise the effect is like mixing hemispherical and spherical representations of the data, and meaningless S^* and R^* values result.

The Moment of Inertia

The moment of inertia provides a third measure of fracture orientation data (Mardia, 1972; Fisher et al., 1987). It readily indicates whether the orientation data are distributed in a unimodal, girdle, or uniform fashion (Figure 8). In a unimodal distribution (Figure 8A), the poles are clustered along one direction, and the moment of inertia about an axis in that direction is small. A single set of parallel fractures yields a unimodal distribution on a hemisphere. In an equatorial distribution poles cluster along a great circle (Figure 8B), and the moment about the axis normal to the equatorial plane is large. The poles to bedding planes in folded rocks commonly form an equatorial distribution. In a uniform distribution (Figure 8C) the poles have no preferred orientation, and the moment about one axis is the same as another. The chaotic fracture orientations in some fault zones resemble uniform distributions.

The following treatment of the moment considers points of unit mass at the endpoints of poles of unit length. The ith point is represented by the unit vector c_i (Figure 9). The direction cosines of c_i are u_i, v_i, and w_i. The moment of inertia M is taken about an axis whose direction is given by the unit vector C with direction cosines U, V, and W. The moment of inertia of the ith point about the axis is defined as the square of the distance a_i between the point and the axis:

$$M_i = a_i^2 \qquad \text{Eq. 7}$$

By the Pythagorean theorem:

$$M_i = a_i^2 = c_i^2 - b_i^2 \qquad \text{Eq. 8}$$

where c_i is the length of c_i, and b_i is the length of the projection of c_i onto C (Figure 9). Equation 8 also can be written using vector notation as:

$$M_i = (c_i \cdot c_i) - (c_i \cdot C)^2 \qquad \text{Eq. 9}$$

Table 1. *Values of ρ, R^*, S^*, and normalized eigenvalues for five fracture pole distributions, listed by increasing value of S^*_h.*

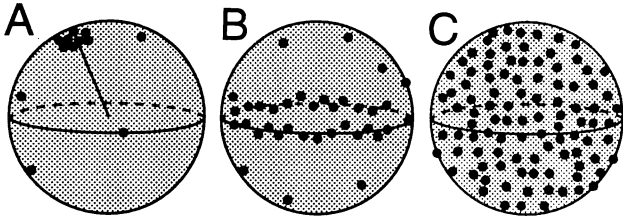| Pole Distribution	ρ	R^*_s	S^*_s	R^*_h	S^*_h	$\bar{\tau}_1$	$\bar{\tau}_2$	$\bar{\tau}_3$	$\bar{\beta}_1$	$\bar{\beta}_2$	$\bar{\beta}_3$
Vertical	∞ if $\|\gamma^*\| = 90°$ 0 if $\|\gamma^*\| \neq 90°$	0	1	1	0	1	0	0	1/2	1/2	0
Biased Uniform	$\cos\gamma^*/\pi$	0	1	2/3	1/3	1/2	1/4	1/4	3/8	3/8	1/4
Random Trend and plunge	$\dfrac{1}{\pi^2 \sin\gamma^*}$	0	1	$2/\pi$	$1-2/\pi$	1/2	1/4	1/4	3/8	3/8	1/4
Uniform	$\dfrac{1}{2\pi}$	0	1	1/2	1/2	1/3	1/3	1/3	1/3	1/3	1/3
Equatorial	—	0	1	0	1	1/2	1/2	0	1/2	1/4	1/4

Figure 8. Distributions of poles: A) unimodal distribution; B) equatorial distribution; C) uniform distribution.

or, because c_i is a unit vector, as:

$$M_i = 1 - (\mathbf{c_i} \cdot \mathbf{C})^2 \qquad \text{Eq. 10}$$

The cumulative moment of all n points is the sum of the individual moments, so in light of Equations 9 and 10 the total moment can be written either as:

$$M = \sum_{i=1}^{n} 1 - \sum_{i=1}^{n} (u_iU + v_iV + w_iW)^2 \qquad \text{Eq. 11}$$

or

$$M = n - \sum_{i=1}^{n} (u_iU + v_iV + w_iW)^2 \qquad \text{Eq. 12}$$

The total moment also can be cast using matrix algebra:

$$M = \mathbf{C}'(n\mathbf{I} - \mathbf{T})\mathbf{C} \qquad \text{Eq. 13}$$

where $\mathbf{I}$ is a 3x3 identity matrix, and $\mathbf{T} = (t_{ij})$ is a 3x3 orientation matrix containing the sums of products of the direction cosines associated with the pole vectors $\mathbf{c_i}$:

$$\mathbf{T} = \begin{bmatrix} \sum_{i=1}^{n} u_i^2 & \sum_{i=1}^{n} u_iv_i & \sum_{i=1}^{n} u_iw_i \\ \sum_{i=1}^{n} u_iv_i & \sum_{i=1}^{n} v_i^2 & \sum_{i=1}^{n} v_iw_i \\ \sum_{i=1}^{n} u_iw_i & \sum_{i=1}^{n} v_iw_i & \sum_{i=1}^{n} w_i^2 \end{bmatrix} \qquad \text{Eq. 14}$$

The 3x1 column vector $\mathbf{C}$ gives the orientation of the axis, and $\mathbf{C}'$ is the 1x3 row vector that is the transpose of $\mathbf{C}$. Noting that:

$$\mathbf{C}'n\mathbf{I}\mathbf{C} = n(U^2 + V^2 + W^2) = n \qquad \text{Eq. 15}$$

one can demonstrate quickly that Equations 12 and 13 indeed are equivalent. An alternative expression of Equation 13 is:

$$M = \mathbf{C}'(\mathbf{B})\mathbf{C} \qquad \text{Eq. 16}$$

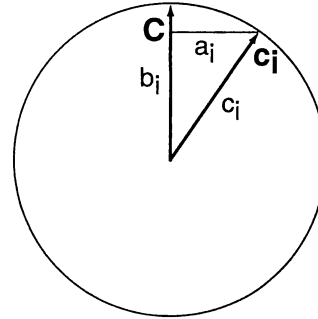where the moment of inertia matrix $\mathbf{B} = (n\mathbf{I} - \mathbf{T})$.

Figure 9. Diagram showing quantities used to define the moment of inertia. $\mathbf{C}$ is the axis about which the moment is taken, and $\mathbf{c_i}$ (in bold) is the unit length pole to a fracture.

The form of Equations 12 and 13 reveal some important aspects of the moment of inertia. First, the moment can be decomposed into separate terms associated with the number of poles (n), the orientation of the axis about which the moment is taken ($\mathbf{C}$), and orientation of the poles ($\mathbf{T}$). The information on the orientation of the poles is contained completely and solely in orientation matrix $\mathbf{T}$. Second, $\mathbf{T}$ and M do not depend on whether the poles are distributed on a hemisphere or a sphere. The reasoning is as follows. If the lower hemisphere representation of a pole were $\mathbf{c_i} = (u_i, v_i, w_i)$, then the corresponding upper hemisphere representation is $\mathbf{c_i}' = (-u_i, -v_i, -w_i)$, so by Equation 14 all the products in $\mathbf{T}$ will have the same sign and magnitude independent of the pole representation format. This behavior of $\mathbf{T}$ contrasts sharply with the spherical variance and resultant direction, which depend strongly on the representation of the poles.

The three eigenvectors and three eigenvalues of moment matrix $\mathbf{B}$ bring the underlying form of a pole distribution into focus. Let β_1, β_2, and β_3 be the maximum, intermediate, and minimum eigenvalues (principal moments) of $\mathbf{B}$, respectively, with $\mathbf{b_1}$, $\mathbf{b_2}$, and $\mathbf{b_3}$ being the corresponding eigenvectors (principal directions). The principal moments β_i can be calculated readily from the eigenvalues (τ_i) of $\mathbf{T}$. First, an inspection of Equations 12, 13, and 15 shows that the trace of $\mathbf{T}$ equals the number of points n:

$$t_{11} + t_{22} + t_{33} = n \qquad \text{Eq. 18}$$

It follows that the sum of the eigenvalues of $\mathbf{T}$ also equals n:

$$\tau_1 + \tau_2 + \tau_3 = n \qquad \text{Eq. 19}$$

where $\tau_1 \leq \tau_2 \leq \tau_3$. Second, in light of the relationship between the components of $\mathbf{B}$ and $\mathbf{T}$:

$$\beta_i = n - \tau_i \qquad \text{Eq. 20}$$

where $\beta_1 \geq \beta_2 \geq \beta_3$. Equations 19 and 20 then yield:

$$\beta_1 + \beta_2 + \beta_3 = 2n \qquad \text{Eq. 21}$$

The τ eigenvalues are usefully normalized by the number of points n ($\bar{\tau}_i = \tau_i / n$) with the β eigenvalues being normalized by $2n$ ($\bar{\beta}_i = \beta_i /2n$). Each set of normalized eigenvalues sum to one.

The normalized eigenvalues for five axisymmetric pole distributions are presented in Table 1, with the supporting calculations in Appendix D. At least two of the three normalized principal moments are equal for these axisymmetric distributions. For a unimodal distribution, such as the first three rows of Table 1, the poles are clustered in the direction of $\mathbf{b_3}$, which has the smallest associated principal moment (β_3). For a single set of parallel fractures, $\bar{\beta}_3$ is distinctive, equaling zero, and $\mathbf{b_3}$ coincides with the pole to the fractures. Surprisingly, the normalized eigenvalues for a biased uniform distribution match those for a distribution where pole trends and plunges are chosen at random, even though the respective R^* and S^* values differ. The match occurs because the smallest moments are equal; axisymmetry and the interdependence of the eigenvalues (Equation 21) require the other two values then to match as well. For a uniform distribution, the normalized principal moments are equal. For an equatorial distribution, the first principal moment is twice the second and third moments. Different distributions thus can have the same eigenvalues and eigenvectors, so two statistical tests are considered for examining fracture orientation data.

STATISTICAL COMPARISON OF MODELS AND DATA

Two statistical treatments are used here to quantify differences between model predictions and observed fracture orientation distributions: the chi-square test and the Kolmogorov-Smirnov test. These tests provide ways to examine differences between observations and a model that S^*, R^*, and eigenvalues do not.

Chi-square Test

The chi-square test is a standard method for comparing two sets of discrete data or for comparing discrete data to continuous data (Davis, 1986; Press et al., 1990). It is used here to compare discrete fracture orientation data with a continuous distribution.

Chi-square tests require subdividing the sets being compared into bins. Let Q_i and q_i be the number of points observed and expected, respectively, in the ith bin, where the total number of bins equals k. Values of Q_i are integers, but values of q_i need not be. The chi-square statistic is calculated as (Fisher et al., 1987; Press et al., 1990):

$$\chi^2 = \sum_{i=1}^{k} \left[(Q_i - q_i)^2 / q_i \right] \qquad \text{Eq. 22}$$

A small value of χ^2 indicates that the two populations can not be distinguished (i.e., the hypothesis cannot be rejected that the differences between the populations are due to random effects), whereas a large value of χ^2 indicates that two populations most likely represent different distributions (Kreyszig, 1983). The bins should be sized such that for no bin is $q_i = 0$; ideally q_i should be greater than five (Hoel, 1963). The number of degrees of freedom, v, is one less than the number of bins k. Ideally k also should not be less than five (Hoel, 1963; Fisher et al., 1987, pp. 76–77).

A key factor in conducting a chi-square test is determining the bins in a consistent and useful manner. Appendix E and Figure 6 show how to partition a lower hemisphere such that an equal number of points is expected in ring-like bins for: a) a uniform distribution, b) a biased uniform distribution, and c) a distribution where pole trends and plunges are chosen at random.

A series of chi-square tests were conducted to compare discrete samples drawn from different distributions with a continuous biased uniform distribution. Several hundred poles were used in the comparisons. In the tests involving a sample drawn from a biased uniform distribution, to no surprise the differences between the populations could be ascribed to random effects. This held when the number of bins was either small (20) or large (100). When a sample of poles with trends and plunges chosen at random was compared to the biased uniform distribution, the chi-square values were typically about two orders of magnitude greater than when a biased sample was compared to the biased uniform distribution. This is interesting given the similarity of R^*, S^*, and the eigenvalues for the two distributions. Apparently the chi-square tests is a more sensitive indicator of differences between populations than the other three measures.

Kolmogorov-Smirnov Test

The Kolmogorov-Smirnov (or K-S) test allows comparisons of *unbinned* distributions of discrete data to a continuous theoretical distribution (Davis, 1986; Press et al., 1990). The test compares the cumulative distribution functions of two distributions, here an observed distribution and a model distribution, that are cast in terms of a single variable. The single variable here is the angle of a fracture pole relative to a borehole (i.e., the apparent co-plunge γ^*). The K-S statistic D is the maximum value of the absolute difference between the two cumulative distribution functions (i.e., D is a measure of the mismatch). A high D value is associated with a low probability $P(D)$ that the differences between the observed and theoretical distributions are due solely to random effects. I refer to the value of γ^* at which D occurs as γ^*_D. At least twenty discrete data points are used to ensure that probabilities based on D are significant. The K-S test avoids difficulties associated with binning

continuous data and so has an advantage over the chi-square test. The K-S test also is more sensitive than the chi-square test to deviations in the parts of distributions where probability densities are low (Davis, 1986), such as where fractures are nearly parallel to a borehole.

FRACTURES FROM STRIPA, SWEDEN

The methods discussed above are applied now to fractures at the Stripa mine in Sweden. Stripa hosted a series of international large-scale rock mechanics experiments from the 1970s to early 1990s (Organization for Economic Co-operation and Development, 1994). Much of the research revolved around rock mass characterization and methods for constructing nuclear waste storage vaults. Numerous experiments addressed fluid flow along fractures and the geophysical characteristics of fracture zones. The in situ distribution of fractures thus was relevant to many research efforts at Stripa.

A series of geophysical experiments and fluid flow tests were conducted at the SCV block (Figure 10). The boundaries of the SCV block were defined to form a cube, centered 355 m below the ground surface, with edges

150 m long. A right-handed coordinate system described locations in this block. The x-, y-, and z-directions corresponded to mine north, mine east, and down, respectively; mine north was 10° west of true north. The mine level exceeded the depth below the surface by 30 m (McKinnon and Carr, 1990, p. 7), so, for example, the 360 level was 330 m below the surface. Several tunnels transected margins of the SCV block, and several borehole arrays extended from these tunnels into the block.

Geologic, geophysical, and hydrologic data gathered from the boreholes and tunnels were used to identify several fracture zones within the SCV block (Black et al., 1990): zones A, B, H, Hb, I, M, and K (Figure 10). Zones A and B strike ~N45E and dip 40°–50° to the southeast. Zones H, Hb, and I strike roughly N5W and dip 63°–76° to the east. Zones M and K strike N60W and dip 65°–87° to the northeast.

Zone H probably is the largest fracture zone, and Black and others (1990) considered it to extend to the surface. Zone H was the best-characterized fracture zone at the site, being pierced by three tunnels and several boreholes. Observations of zones H and Hb in the tunnel walls
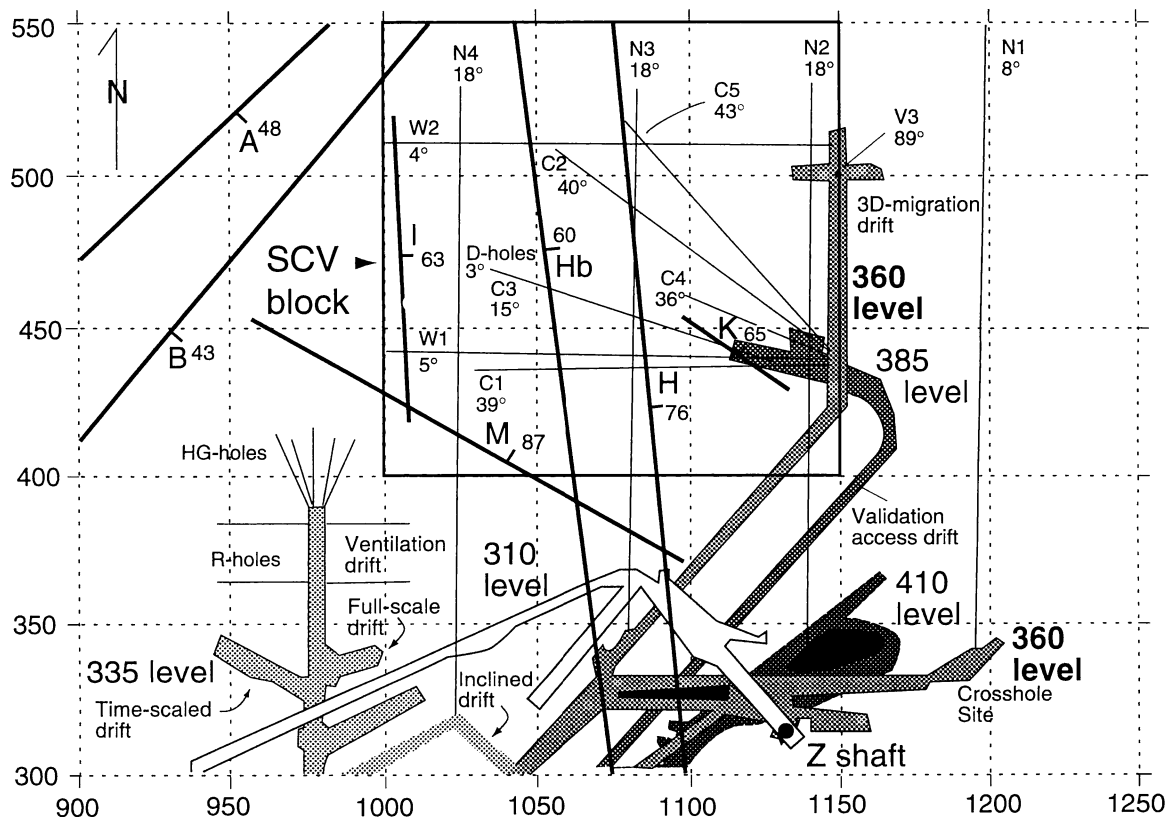

Figure 10. Map showing the location of drifts (outlined/shaded), boreholes (light lines), and fracture zones (heavy lines) near the SCV block at the Stripa mine. Boreholes and drifts are projected orthogonally onto the horizontal plane. The fractures zone traces are shown where they would intersect the 360-m level of the mine. Angles denote overall inclination of the boreholes. Borehole C3 is not shown; it projects along the line of the D-holes. The north arrow points in the direction of mine north, not true north. The reference grid (in meters) for the mine is shown also.

showed no discernible boundary between the zones (Martel, 1992), and they are considered in the remainder of this report to be part of the same zone. Based on contour plots of fracture pole data obtained from boreholes piercing zone H, Gale and others (1990) concluded that the zone contained a pronounced set of steep, north-striking fractures and a more weakly defined set of subhorizontal fractures. Driftwall exposures of zone H revealed short fractures of many orientations, whereas the longest fractures parallel the zone as a whole and are faults (Martel, 1992). Scanline data were not collected for fractures with trace lengths less than 0.5 m, however (Gale et al., 1990); this would have required an inordinate amount of time owing to the great number of fractures.

Many of the fractures with trace lengths of less than 0.5 m that branch from the faults of zone H most likely formed as a result of fault slip (see Martel et al., 1988; Martel, 1990). The highly varied orientations of these short fractures probably reflect many different senses of slip along the faults (Martel, 1992). Examinations of these fractures were important in understanding the mechanics and kinematics of faulting at Stripa, even though these fractures were not part of the scanline data.

Gale and his co-workers used cluster analyses (e.g., Priest, 1985) of borehole and scanline data to characterize the gross orientation distribution of individual fractures within the SCV block. Based on preliminary data, Gale and Stråhle (1988) concluded: a) that fractures could be grouped into three major clusters (one steeply-dipping set that strikes N-S, another that strikes NW, and a subhorizontal set), and b) that "the north-south striking fracture set has a much higher density than the other sets or clusters." Gale and others (1990) analyzed a larger data set and inferred that the fractures fell into one large cluster (N-S strike), one intermediate-size cluster (WNW strike), and ten small clusters. They also noted that the orientation data did not define these fracture sets very crisply.

My approach to analyzing fractures in the SCV block differs from that of Gale and co-workers. First, a model of fracturing in and adjacent to zone H is constructed based on geologic data and geomechanical concepts. That model then is tested against borehole observations. The goal is not to produce a perfect reference model, but rather to see how the observations depart from the model. Second, rather than using cluster analysis, I describe explicitly how the in situ distribution of fractures is affected by borehole bias and analyze the data in terms of spherical mean direction, spherical variance, and principal moments of inertia.

Analysis

My reference model is a uniform orientation distribution. It is motivated by the numerous fracture orientations observed in the driftwalls and boreholes and by

evidence for several senses of slip along the north-striking faults (Martel, 1992). This model does not contain a concentration of fault zone-parallel fractures, but it is consistent with the secondary fracturing one might expect along a fault zone that had been reactivated repeatedly under varied stress conditions. Gale and co-workers provided the fracture orientation data.

Figures 11, 12, 13, and 14 compare observed fracture orientations from the W, N, C, and D boreholes, respectively, with model predictions. The predictions were obtained in the manner of Figure 7, with the number of fractures in a given model plot matched to the number of fractures in the corresponding observed distribution. These figures reveal three key points. First, the data reveal a broad range of fracture orientations in the SCV block. Second, the model results are grossly similar to the respective observations for nearly all of the boreholes. The observations reveal a diffuse cloud of fracture poles clustered about the orientation of the respective borehole. This pattern holds no matter what the orientation of the hole. The gross similarity between observations and predictions suggests that fractures in the SCV block are oriented in a largely uniform manner, with the observed distributions being strongly influenced by borehole bias. Third, the degree of similarity between observations and predictions, especially with regard to the degree of clustering, varies depending on the orientation of a borehole. The match is best for the N holes (Figure 12), with the N4 observations best resembling the predictions of the biased uniform model. The N holes do not
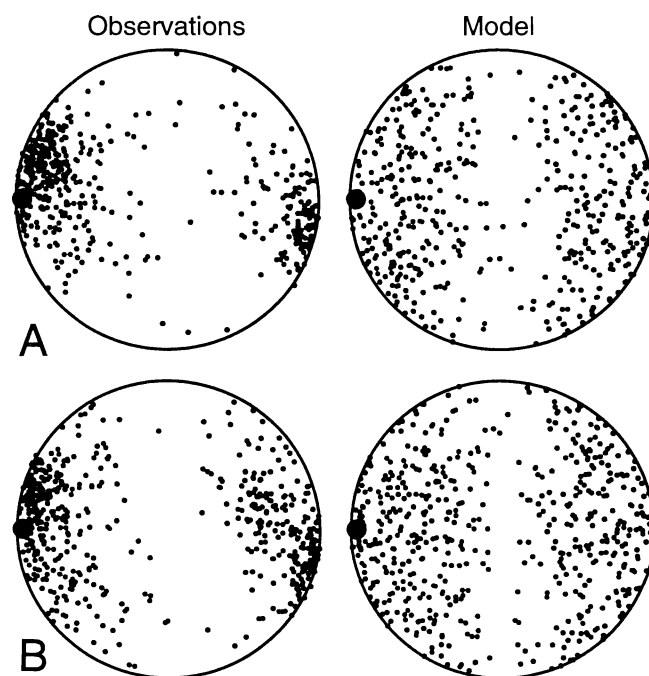
Observations   Model

Figure 11. Equal area projections of poles to fractures observed (left) and modeled (right) in the W-holes at the SCV block: A) W1; B) W2. In this figure, and the next three, borehole orientations are shown by heavy dots.

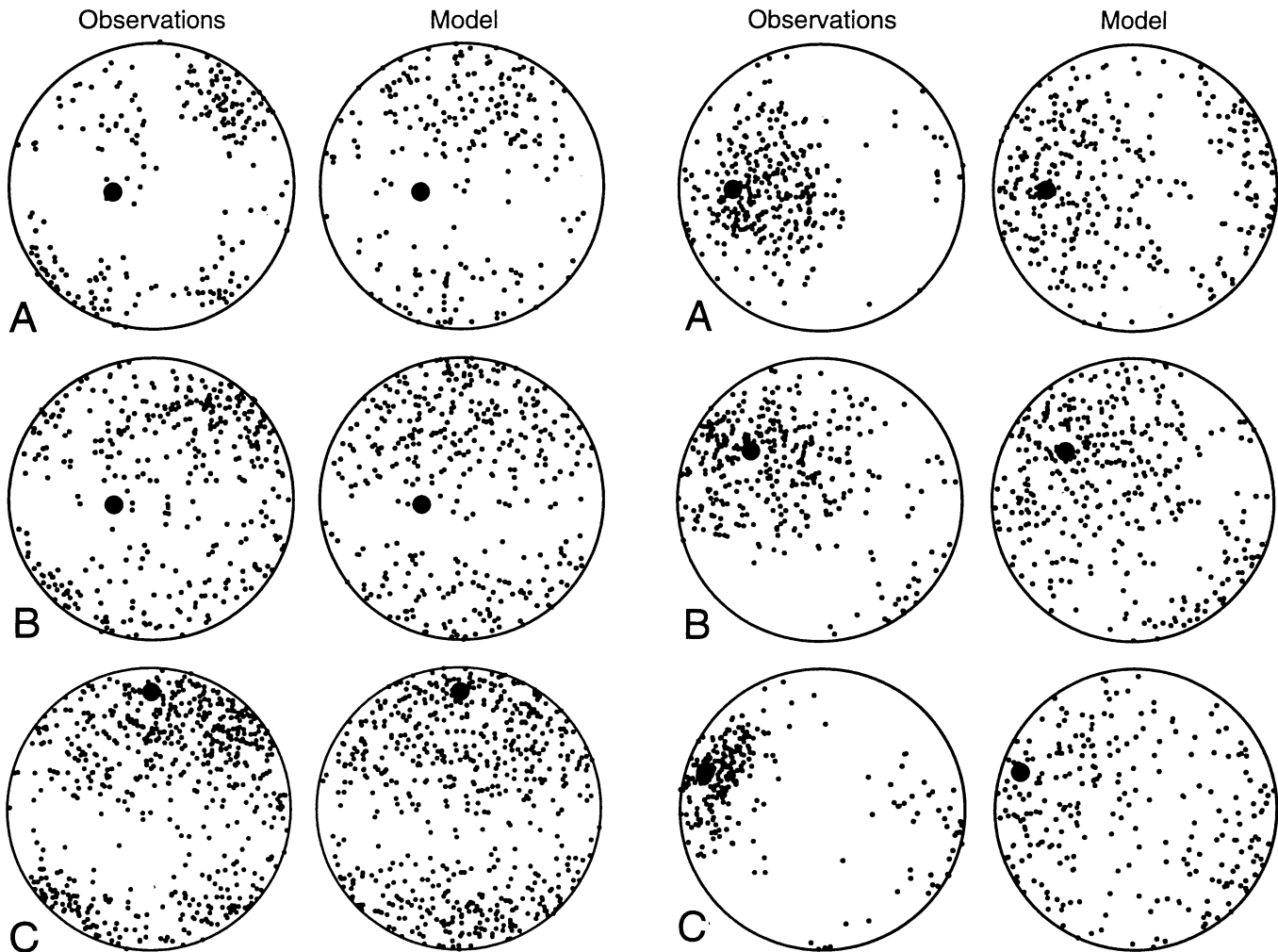Observations   Model   Observations   Model

Figure 12. Equal area projections of poles to fractures observed (left) and modeled (right) in the N-holes at the SCV block: A) N2; B) N3; C) N4.

penetrate zone H (Black et al., 1990). For all the other holes, which do penetrate zone H, the observed poles clearly cluster more tightly about the respective borehole than the model predicts (see Figures 11, 13, and 14). All of these holes have westerly trends, relatively gentle inclinations, and intersect a distinctly higher proportion of fractures with northerly strikes and steep dips than a uniform *in situ* model predicts. These observations suggest that the orientations of fractures in the SCV block outside zone H are distributed in a rather uniform manner, whereas north-striking fractures are more highly concentrated in zone H.

A review of the fracture orientation measures, summarized in Table 2, bears out these conclusions. Figure 15 shows S^* values for data from the various holes. The N-holes show S^* values most consistent with sampling from a uniform *in situ* distribution ($S^* \approx 1/3$). The other holes reveal significantly less scatter, especially the D-holes. Figure 16 shows that the resultant pole orientations are close to the orientation of the respective borehole.
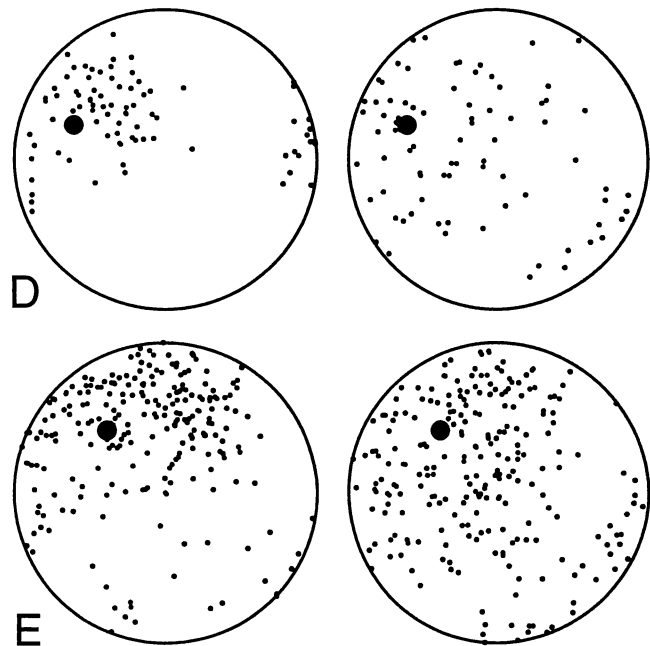

Figure 13. Equal area plots comparing poles for observed (left) and modeled (right) fracture orientations from the C-holes: A) C1; B) C2; C) C3; D) C4; E) C5.
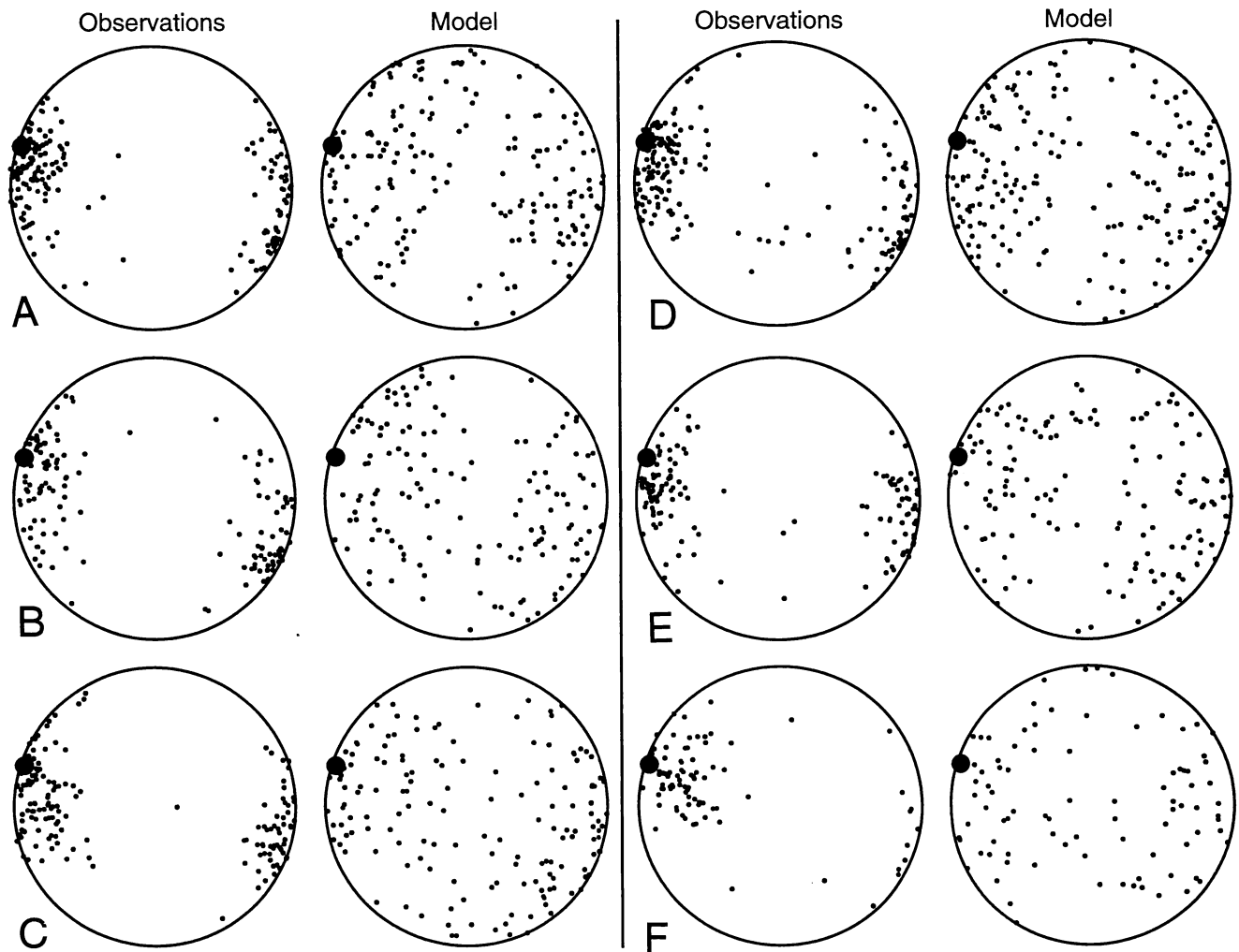
Figure 14. Equal area plots comparing poles for observed (left) and modeled (right) fracture orientations from the D-holes: A) D1; B) D2; C) D3; D) D4; E) D5; F) D6.

For five D-holes, however, the resultants trend slightly west of the holes, whereas for the C- and N-holes the resultants plot slightly to the east. This reflects the presence of more steep, north-striking fractures in those holes than a random distribution would yield. The same pattern shows up in the orientation of the axis for the smallest moment (Figure 17). Figure 18 shows the ratios of normalized principal moments (eigenvalues), respectively. Data for the N-holes once again most closely reflect a uniform biased distribution. Data from the other holes reveal a mixture of uniform, unimodal, and girdle components, with the unimodal component generally becoming more pronounced for the boreholes that completely penetrate zone H/Hb.

Chi-square statistics (Table 3, Figure 19), calculated for 19 degrees of freedom, reflect a similar pattern: the best fit (lowest χ^2 values) to a uniform distribution occurs for the N-holes, and the worst fit for the W-holes. The chi-square values for all the holes, including the N-holes, are well above the range of 30 to 45 at which the differences can be attributed solely to random effects (Fisher

et al., 1987). All the data sets contain a statistically significant non-uniform component.

The K-S tests provide additional quantitative insight into the fracture distribution. Figure 20 shows representative cumulative distribution functions for six of the sixteen holes. The W1, C1, and D1 data plot everywhere above the theoretical curves for a biased uniform distribution (Figure 20A, D, and F). The mismatch between the functions on those plots increases with increasing γ^* for angles less than γ^*_D, and decreases for greater angles. This means that, relative to a uniform *in situ* distribution, the fracture poles of the W1, C1, and D1 data are concentrated for γ^* less than 34°, 51°, and 35°, respectively, and are relatively sparse at greater angles. This quantitative conclusion is not readily obtained from a casual inspection of the equal area plots, especially for an inclined hole such as C1 (Figure 13A). The clustering is apparent in Figures 11A, 13A, and 14A, and it reflects a concentration of steep north-striking fractures. In contrast, the N3 data (Figure 20B) plot everywhere below the theoretical curves for a biased uniform

Table 2. *Eigenvectors and normalized eigenvalues for moments for fracture poles detected by the SCV boreholes.*

Hole	Hole trend	Hole plunge	$\overline{\beta}_1$	$\overline{\beta}_2$	$\overline{\beta}_3$	b_1 trend	b_1 plunge	b_2 trend	b_2 plunge	b_3 trend	b_3 plunge
W1	270.6	4.7	0.454	0.436	0.110	188.4	8.3	60.3	76.7	280.0	10.3
W2	270.5	4.1	0.436	0.422	0.142	182.8	30.8	9.7	59.1	274.6	3.0
N2	0.5	18	0.413	0.372	0.215	229.2	78.1	124.2	3.1	33.6	11.5
N3	1.1	17.7	0.399	0.352	0.249	213.4	70.6	121.2	0.8	30.9	19.4
N4	0.6	18.3	0.405	0.354	0.241	193.5	68.0	293.5	4.0	25.1	21.6
C1	268.6	38.1	0.430	0.425	0.145	156.1	13.7	57.2	32.5	265.8	54.1
C2	305.9	40.4	0.428	0.388	0.184	201.0	16.1	95.1	43.4	306.1	42.2
C3	288.2	14.7	0.456	0.438	0.107	173.8	51.4	31.8	32.2	289.3	19.0
C4	290.9	35.6	0.461	0.379	0.161	180.1	34.0	62.3	34.7	300.7	37.1
C5	317.6	42.7	0.424	0.380	0.196	184.8	51.5	85.1	7.6	349.2	37.5
D1	287.9	3.3	0.467	0.456	0.077	52.4	80.8	187.9	6.6	278.6	6.4
D2	287.8	3.3	0.458	0.443	0.099	24.2	64.9	192.4	24.6	284.5	4.5
D3	287.6	3.1	0.471	0.444	0.085	14.2	44.0	182.4	45.4	278.4	6.0
D4	287.8	3.5	0.462	0.441	0.097	19.1	38.8	181.9	49.9	282.2	8.6
D5	287.9	3.4	0.462	0.453	0.086	8.3	19.1	171.5	70.1	276.5	5.4
D6	288	3.2	0.466	0.450	0.084	28.8	27.0	161.7	53.1	286.3	23.1

distribution. The N3 poles are relatively sparse for γ^* less than 50° and are relatively concentrated at greater angles. This nonuniformity is not obvious in Figure 12C, but it is reflected in the distribution of principal moments (see Figure 18). Figure 18 shows that the N3 data reflect a distinct secondary contribution from a girdle component, rather than just a unimodal component. This component reflects fractures with a northerly strike and a range of dips. These might have developed in response to dip slip along north-striking faults (Martel, 1992). The N4 and C5 data (Figure 20C and E) hug the theoretical curves, meandering above and below them. For N4, the model and observations match well for $\gamma^*<16°$ and $\gamma^*>51°$, poles are concentrated between 16° and 42°, and poles are relatively sparse between 42° and 51°. For C5, the model and observations match well for $\gamma^*<40°$, poles are concentrated between 40° and 51°, and poles are relatively sparse between 51° and 75°. Finally, Table 3 shows that the D-values for all data sets correspond to a low probability P that the boreholes sample a uniform

distribution *in situ*. Table 3 also shows the smallest mismatch between the data and a uniform *in situ* distribution for the N-holes, consistent with the results of the chi-square test, the R^* and S^* values, and the results of Figure 18. In general, D and χ^2 increase as the unimodal character of the data increases (Figure 18). The plots of the cumulative distribution functions (Figure 20), however, are much more useful than the D-values alone for characterizing departures of the data from the model.

The comparisons thus suggest that the SCV fractures have both a uniform component and a component of steeply-dipping fractures that strike north, roughly parallel to zone H. The N-holes indicate the uniform component is most pronounced outside zone H, and the other holes indicate the zone-parallel component is most pronounced within zone H. This pattern is consistent with the fracturing having accompanied repeated slip along steep north-striking faults during distinctly different episodes of deformation, and with the north-striking faults
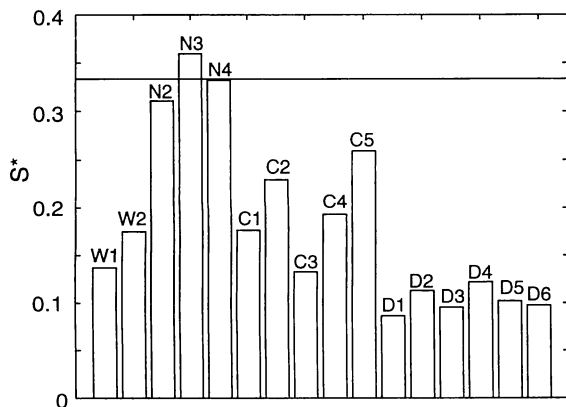

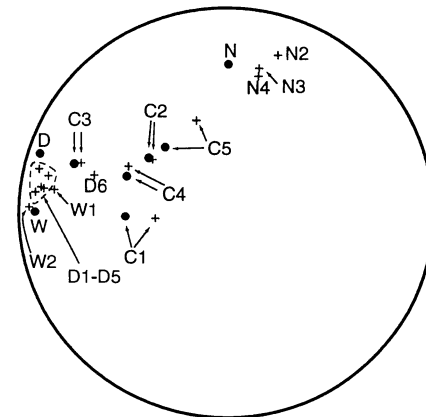Figure 15. Histogram showing S^* values for fracture orientation data from the N,W,C, and D-holes.

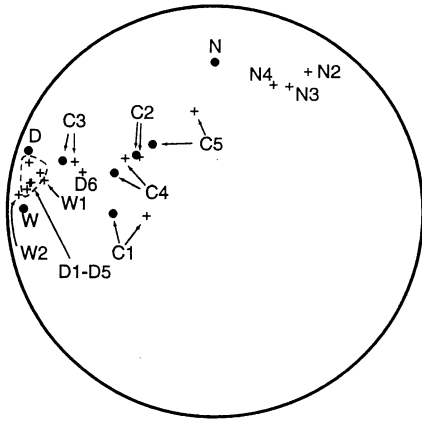Figure 16. Equal-angle (stereographic) plot showing orientation of the resultant (+) for each SCV borehole (•).

Figure 17. Equal-angle (stereographic) plot showing orientation of the axis of the smallest moment (+) for each SCV borehole (•).

Figure 19. Histogram showing χ^2 value for each SCV borehole as compared to a uniform distribution affected by borehole bias.

being concentrated in zone H. The borehole data are thus compatible not only with the driftwall observations but also with the inferred history of faulting and fracturing at the mine.

DISCUSSION

The conclusions reached here regarding the orientations of fractures in the SCV block are compatible with those of Gale and Stråhle (1988) and Gale and others (1990) but have a slightly different emphasis. As is found here, Gale and his co-workers detected fractures of numerous orientations and concluded that steep, north-striking fractures formed the most prominent set. Their cluster analysis indicated eleven subsets of fracture orientations (Gale et al., 1990), but they noted that those sets were not sharply defined and directly reflected limitations in the method of sampling. They concluded that two fracture clusters were more appropriate, one set representing fractures that strike to the north, the other set containing fractures that strike to the northwest. Dispersion of fractures within these sets is necessary to
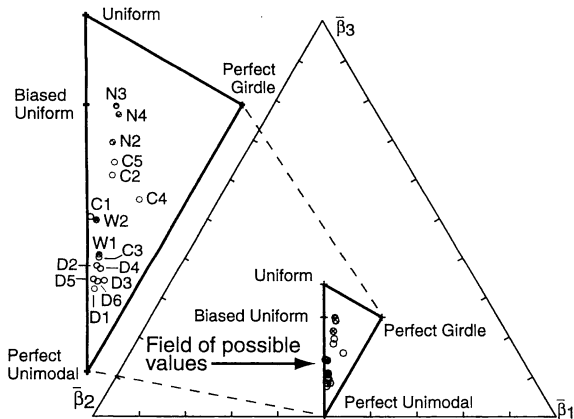

Figure 18. Ternary diagram showing normalized principal moments for fracture orientation data from the N-, W-, C-, and D-holes.
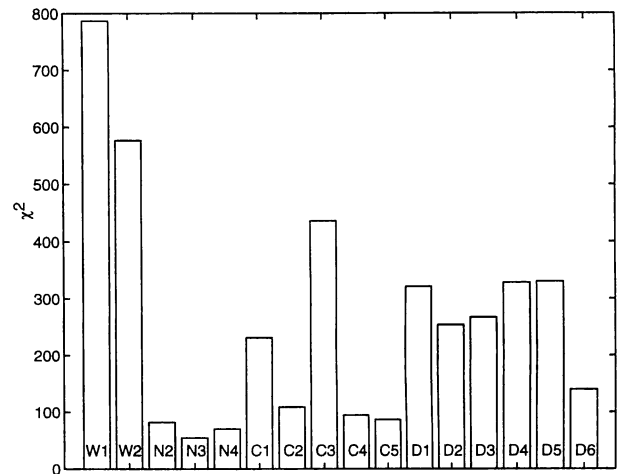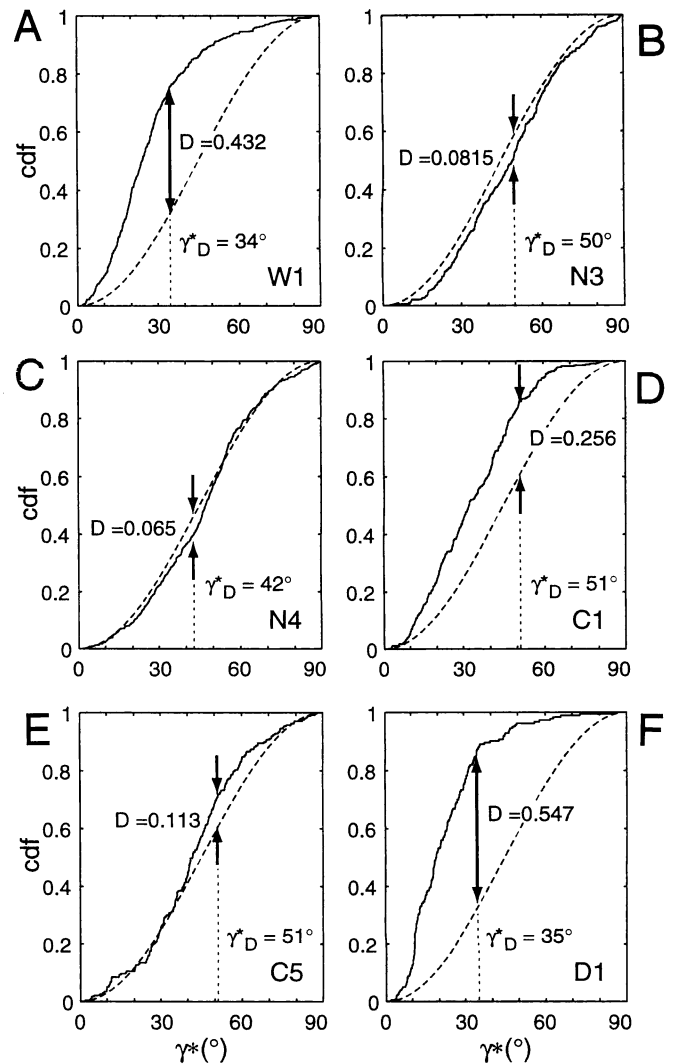

Figure 20. Representative cumulative distribution functions for data from six boreholes: A) W1; B) N3; C) N4; D) C1; E) C5; F) D1. Data are shown by solid curves. Theoretical curves for a biased uniform model are dashed.

Table 3. Spherical variance (S*), normalized resultant length (R*), resultant trend and plunge, χ^2 values, D-values, and probabilities P(D) for fracture pole data from the SCV boreholes. The probabilities reflect the likelihood that the observations differ from a biased uniform model due solely to random effects.

Hole	Hole trend	Hole plunge	S*	R*	Trend$_R$	Plunge$_R$	χ^2 (20 bins)	D	P(D)
W1	270.7	4.7	0.137	0.863	278.2	10.1	786.6	0.4323	1.31e-80
W2	270.6	4.1	0.175	0.825	272.1	2.9	576.7	0.3375	3.31e-57
N2	0.5	18.0	0.311	0.690	17.7	12.1	81.8	0.1282	0.0012
N3	1.1	17.7	0.360	0.640	12.3	18.3	54.3	0.0815	0.0138
N4	0.6	18.3	0.332	0.668	12.7	21.2	70.0	0.0649	0.0113
C1	268.6	38.1	0.176	0.824	266.3	52.1	231.1	0.2555	6.22e-20
C2	305.9	40.4	0.230	0.770	306.4	42.2	108.8	0.2094	1.49e-14
C3	288.2	14.7	0.133	0.868	289.4	16.9	436.3	0.4966	1.50e-56
C4	290.9	35.6	0.193	0.807	296.0	34.6	94.6	0.2993	8.33e-07
C5	317.6	42.7	0.259	0.741	342.1	39.1	86.6	0.1132	0.0044
D1	287.9	3.3	0.086	0.914	278.0	6.8	321.2	0.5470	3.08e-48
D2	287.8	3.3	0.113	0.887	283.5	4.3	254.0	0.4709	2.34e-28
D3	287.6	3.1	0.096	0.905	278.3	5.9	267.3	0.4908	7.34e-33
D4	287.8	3.5	0.122	0.878	282.1	7.5	328.1	0.4965	2.19e-42
D5	287.9	3.4	0.102	0.898	276.7	4.4	329.9	0.5215	1.95e-34
D6	288.0	3.2	0.098	0.903	286.5	22.9	139.7	0.4037	6.98e-13

account for the variety of orientations observed. The somewhat simpler interpretation presented here is that one prominent set strikes nearly north-south and dips steeply, and that the other fractures collectively represent a nearly uniform distribution of fracture orientations. This model is consistent with the data I am aware of.

Heterogeneity in the spatial distribution of fractures complicates interpretation of the borehole data. For example, even though the N4 hole was only about 6 percent longer than N2 (219 m versus 207 m), it intersected almost three times as many fractures (Figure 12). These holes are parallel and spaced about 115 m apart. Even among the D-holes, which are parallel, the same length, and are spaced within 2 m of one another, the number of fractures intersected varies by more than a factor of two (Figure 13). The fracture distribution clearly is heterogeneous spatially. One could argue on philosophical grounds that, given the spatial inhomogeneity and complications from borehole bias, the model proposed here might be preferable to the model of Gale and others (1990) because it is simpler. The differences between the models appear small, however, and might prove insignificant in a rigorous comparison.

Differences between the approaches are more significant than differences between the models. The study here was motivated by a desire to understand the fracture distribution data in light of the inferred geologic history. Information on the geologic history was used directly in preparing a forward model, and that was analyzed with relatively simple statistical methods. Gale and his co-workers were motivated primarily to characterize the SCV block from a statistical sense and applied a much more sophisticated statistical analysis. The availability of good exposures, excellent borehole data, and, ironically, the complicated geology allowed both approaches to

converge on similar models for the fracture distribution within the SCV block.

Gale and his co-workers emphasized the need to carefully collect and analyze borehole orientation data in order to avoid introducing errors into an analysis of fracture orientation data. This point should not be taken lightly. A variety of errors can compound or obscure borehole bias effects. Orientation errors can be introduced in evaluating the orientations of fractures on televiewer or borehole camera logs. Errors can also be introduced when fracture orientations are measured in cores and when these measurements are transformed to give the *in situ* orientations.

Finally, the *in situ* orientations of individual segments of core must be determined accurately in order to properly transform the fracture orientation data obtained from core measurements, and this is not a trivial matter. Core orientation errors will tend to randomize the orientation data, increasing the difficulty of detecting fracture sets in largely chaotic fracture distributions.

CONCLUSIONS

Fracture orientation data from a borehole invariably are biased. *In situ* fractures at low angles to the borehole are under-represented. For a continuous uniform *in situ* distribution of fractures sampled by a borehole, the mean hemispherical orientation of fracture poles is along the borehole, and the hemispherical variance is 1/3. The ratio of the principal moments of the fracture poles is 3/8:3/8:1/4, with the eigenvector associated with the smallest principal moment paralleling the borehole. These measures, along with those for unimodal and equatorial distributions, provide useful standards for comparison.

Statistics could also be calculated for other distributions affected by observational bias. A prime candidate is the Watson distribution (Fisher et al., 1987), which describes dispersed girdle and bipolar (unimodal) distributions of axial data. The treatment of a biased Watson distribution, however, is rather formidable and beyond the scope of this paper.

By assuming a particular model for the *in situ* distribution of fractures, such as a uniform model, and then correcting for borehole bias, one can predict the distribution of fractures a borehole would encounter. The mismatch between observations and predictions can be evaluated visually, using equal area projections, or quantitatively with chi-square tests or K-S tests.

An analysis of fracture orientation data from a complexly fractured granite at the Stripa mine in Sweden shows that geologic information on the kinematics and mechanics of fracturing can be used in conjunction with fracture orientation data from boreholes to understand the *in situ* fracture distribution. Inspection of fractures in tunnel exposures at Stripa revealed that repeated fracturing occurred along old faults. This resulted in a great variety of fracture orientations, but the most prominent fractures are faults parallel to the fault zones. The fracture orientation statistics for holes that did not pierce the main fault zones are consistent with a biased uniform distribution, whereas those that did pierce the main fault zones show a greater presence of zone-parallel fractures than a uniform distribution would predict. The statistical data thus are consistent with the geologic interpretation of the fracturing history. Many of the fractures used to infer the history of fracturing were sufficiently short that they would not be included in scanline survey records of tunnel walls.

ACKNOWLEDGMENTS

REFERENCES

BLACK, J. H.; OLSSON, O.; GALE, J. E.; AND HOLMES, D. C., 1990, *Site Characterization and Validation-Stage 4 Preliminary Assessment and Detail Predictions:* Stripa Project technical report 91-08.

DAVIS, J. C., 1986, *Statistics and Data Analysis in Geology:* John Wiley and Sons, New York, 646 p.

FISHER, N. I.; LEWIS, T.; AND EMBLETON, B. J. J., 1987, *Statistical Analysis of Spherical Data:* Cambridge University Press, Cambridge, U.K., 329 p.

GALE, J. AND STRÅHLE, A., 1988, *Site Characterization and Validation - Drift and Borehole Fracture Data, Stage 1:* Stripa Project internal report 88-10.

GALE, J.; MACLEOD, R.; STRÅHLE, A.; AND CARLSTEN, S., 1990, *Site Characterization and Validation-Drift and Borehole Fracture Data, Stage 3:* Stripa Project internal report 90-02.

GELLERT, W.; KÜNSTER, H.; HELLWICH, M.; AND KÄSTNER, H., 1977, *The VNR Concise Encyclopedia of Mathematics:* Van Nostrand Reinhold, New York, 758 p.

GOODMAN, R. E., 1976, *Methods of Geological Engineering in Discontinuous Rocks:* West Publishing Company, St. Paul, MN, 472 p.

GOODMAN, R. E., 1980, *Introduction to Rock Mechanics:* Wiley, New York, 478 p.

HANEBERG, WILLIAM, 1999, written communication, Haneberg Geoscience, 10411 SE Olympiad Drive, Port Orchard, WA 98336.

HOBBS, B. E.; MEANS, W. D.; AND WILLIAMS, P. F., 1976, *An Outline of Structural Geology:* Wiley, New York, 571 p.

HOEL, P. G., 1963, *Introduction to Mathematical Statistics:* Wiley, New York, 428 p.

KREYSZIG, E., 1983, *Advanced Engineering Mathematics:* Wiley, New York, 988 p.

KULANDER, B. R.; DEAN, S. L.; AND WARD, B. J., JR., 1990, *Fractured Core Analysis:* American Association of Petroleum Geologists, Tulsa, OK, 88 p.

MARDIA, K.V., 1972, *Statistics of Directional Data:* Academic Press, New York, 355 p.

MARTEL, S. J., 1990, Formation of compound strike-slip fault zones, Mount Abbot quadrangle, California: *Journal of Structural Geology,* Vol. 12, pp. 869–882.

MARTEL, S. J., 1992, *Geologic Characterization of Fractures as an Aid to Hydrologic Modeling of the SCV Block at the Stripa Mine:* Lawrence Berkeley Laboratory report LBL-32310, 81 p.

MARTEL, S. J.; POLLARD, D. D.; AND SEGALL, P., 1988, Development of simple fault zones in granitic rock, Mount Abbot quadrangle, Sierra Nevada, California: *Geological Society of America Bulletin,* Vol. 100, pp. 1451–1465.

MCKINNON, S. AND CARR, P., 1990, *Site Characterization and Validation—Stress Field in the SCV Block and Around the Validation Drift, Stage 3:* Stripa Project technical report 90-09.

NATIONAL ACADEMY OF SCIENCES, 1996, *Rock Fractures and Fluid Flow: Contemporary Understanding and Applications:* National Academy Press, Washington, DC, 551 p.

ORGANIZATION FOR ECONOMIC CO-OPERATION AND DEVELOPMENT, 1994, *In situ experiments at the Stripa mine, in Proceedings of the Fourth International NEA/SKB Symposium,* Stockholm, Sweden, 14-16 October 1992, Washington, DC, 468 p.

PRESS, W. H.; FLANNERY, B. P.; TEUKOLSKY, S. A.; AND VETTERLING,

W. T., 1990, *Numerical Recipes:* Cambridge University Press, Cambridge, U. K., 702 p.

PRIEST, S. D., 1985, *Discontinuity Analysis for Rock Engineering:* George Allen & Unwin, London, 124 p.

SCHEIDEGGER, A.E., 1965, *On the Statistics of the Orientation of Bedding Planes, Grain Axes and Similar Sedimentological Data,* U.S. Geological Survey Professional Paper 525-C: U. S. Geological Survey, Denver, CO, pp. 164-167.

TERZAGHI, R., 1965, Sources of error in joints surveys: *Geotechnique,* Vol. 15, pp. 287-304.

THE MATHWORKS, 1992, *Matlab Reference Guide:* The MathWorks, Natick, MA, 548 p.

WATSON, G. S., 1965, Equatorial distributions on a sphere: *Biometrika,* Vol. 52, pp. 193–201.

WATSON, G. S., 1966, The statistics of orientation data: *Journal of Geology,* Vol. 74, pp. 786–797.

WOODCOCK, N. H., 1977, Specification of fabric shapes using an eigenvalue method: *Geological Society of America Bulletin,* Vol. 88, pp. 1231–1236.

APPENDIX A
INCREMENTAL AREA ON THE SURFACE OF A SPHERE

If a surface in space can be described using the following parametric expression:

$$u = u\,(\alpha,\gamma), \quad v = (\alpha,\gamma), \quad w = w\,(\alpha,\gamma) \qquad \text{Eq. A1}$$

then the area of a surface is (Kreyszig, 1983):

$$A = \int_{\gamma_1}^{\gamma_2} \int_{\alpha_1}^{\alpha_2} \sqrt{EG - F^2}\; d\alpha\, d\gamma \qquad \text{Eq. A2}$$

where:

$$E = \left(\frac{\partial u}{\partial \gamma}\right)^2 + \left(\frac{\partial v}{\partial \gamma}\right)^2 + \left(\frac{\partial w}{\partial \gamma}\right)^2 \qquad \text{Eq. A3}$$

$$F = \frac{\partial u}{\partial \gamma}\frac{\partial u}{\partial \alpha} + \frac{\partial v}{\partial \gamma}\frac{\partial v}{\partial \alpha} + \frac{\partial w}{\partial \gamma}\frac{\partial w}{\partial \alpha} \qquad \text{Eq. A4}$$

and

$$G = \left(\frac{\partial u}{\partial \alpha}\right)^2 + \left(\frac{\partial v}{\partial \alpha}\right)^2 + \left(\frac{\partial w}{\partial \alpha}\right)^2 \qquad \text{Eq. A5}$$

By substituting the expressions for u, v, and w in Equations 1-1, 1-2, and 1-3 into Equations A3–A5 one obtains:

$$E = 1 \qquad \text{Eq. A6}$$

$$F = 0 \qquad \text{Eq. A7}$$

$$G = \sin^2\gamma \qquad \text{Eq. A8}$$

Substituting the reduced expressions for E, F, and G into Equation A2 yields:

$$A = \int_{\gamma_1}^{\gamma_2} \int_{\alpha_2}^{\alpha_1} \left(\sin\gamma\right) d\alpha\, d\gamma \qquad \text{Eq. A9}$$

So if:

$$A = \int_A dA \qquad \text{Eq. A10}$$

then the element of area dA is given by:

$$dA = (\sin\gamma)d\alpha\, d\gamma \qquad \text{Eq. A11}$$

This agrees with the solution of Priest (1985).

APPENDIX B
PROBABILITY DENSITY FOR POLES ON A HEMISPHERE

Let ρ be the probability density of fracture poles over the surface of a hemisphere. The function ρ is analogous to the function h of Fisher and others (1987) that describes the distribution of points on the surface of a sphere. For a uniform pole distribution, ρ is a constant that equals the reciprocal of the area of a hemisphere of unit radius (i.e., $\rho_{uniform} = 1/2\pi$). Substituting this expression into Equation 6-3 yields the cumulative distribution function (*cdf*) for a uniform distribution in terms of the acute angle between the fracture pole and the borehole axis γ^* (i.e., the ap-parent pole co-plunge):

$$cdf_{uniform} = (1 - \cos\gamma^*) \qquad \text{Eq. B1}$$

For a uniform distribution affected by borehole bias:

$$\rho_{bias} = c\cos\gamma^* \qquad \text{Eq. B2}$$

To find c, one substitutes Equation B2 into Equation 6-3:

$$\int_{\gamma^* = 0}^{\gamma^* = \pi/2} 2\pi \left(c\cos\gamma^*\right)\left(\sin\gamma^*\right) da^* d\gamma^* = 1 \qquad \text{Eq. B3}$$

Solving for c yields:

$$c = 1/\pi \qquad \text{Eq. B4}$$

hence:

$$\rho_{bias} = \cos\gamma^*/\pi \qquad \text{Eq. B5}$$

Substituting this expression into Equation 6-3 yields the cumulative distribution function (*cdf*) for a biased uniform distribution in terms of the apparent pole co-plunge γ^*:

$$cdf_{bias} = \frac{1}{2}\left(1 - \cos 2\gamma^*\right) \qquad \text{Eq. B6}$$

Consider now the case where fracture pole trends and plunges are chosen at random from the intervals 0°–360° and 0°–90°, respectively. The density of poles along any horizontal small circle is inversely proportional to the

circumference, and radius, of the small circle. The radius of the small circle is $\sin\gamma^*$ (Figure 2A), so here:

$$\rho_{random} = c_{random}\frac{1}{\sin\gamma^*} \qquad \text{Eq. B7}$$

Solving for c_{random} using Equation 6-2 yields:

$$c_{random} = \frac{1}{\pi^2} \qquad \text{Eq. B8}$$

hence:

$$\rho_{random} = \frac{1}{\pi^2\sin\gamma^*} \qquad \text{Eq. B9}$$

Substituting this expression into Equation 6-3 yields the cumulative distribution function (*cdf*) for this distribution in terms of the apparent pole co-plunge γ^*:

$$cdf_{random} = \frac{2}{\pi}(\gamma^*) \qquad \text{Eq. B10}$$

APPENDIX C
SPHERICAL VARIANCE

For a series of n discrete unit pole vectors, the spherical variance S^* is defined as:

$$S^* = 1 - R^* \qquad \text{Eq. C1}$$

where R^* is the normalized length of the resultant vector formed by summing all the unit pole vectors. The resultant length is zero for a continuous uniform distribution on a *sphere*. This is a direct consequence of the symmetry of the poles about the center of the sphere.

For a distribution on a lower hemisphere, the maximum value of S^* occurs for a series of vertical fractures with a uniform distribution of strikes. Here $S^* = 1$ and $R^* = 0$. The minimum value of S^* is obtained for a series of horizontal planes. Here $S^* = 0$ and $R^* = 1$.

For a continuous uniform pole density distribution on a lower hemisphere the resultant will point straight down: no poles have an upward component, and the distribution is axisymmetric. Here, S^* is given by:

$$S^* = 1 - \int_A \left(\cos\gamma^*\right)(\rho)\left(dA\right) \qquad \text{Eq. C2}$$

The $\cos\gamma^*$ term is the downward contribution of a given pole, and the ρdA term is a weighting term for poles in area dA. Casting Equation C2 in terms of angles α^* and γ^* yields:

$$S^* = 1 - \int_{\gamma^*=0}^{\gamma^*=\pi/2}\int_{\alpha^*=0}^{\alpha^*=2\pi} \left(\cos\gamma^*\right)(\rho)\left(\sin\gamma^*\,d\alpha^*\,d\gamma^*\right)$$

$$\text{Eq. C3}$$

If $\rho = \frac{1}{2\pi}$ (i.e., the distribution is uniform), then:

$$S^* = 1 - \frac{1}{2} = \frac{1}{2} \qquad \text{Eq. C4}$$

For this case $R^* = 1/2$.

For a biased uniform distribution $\rho = (1/\pi)\cos\gamma^*$ (Equation B4). This distribution is axially symmetric about a borehole. Solving Equation C3 for this case yields:

$$S^* = 1 - \frac{2}{3} = \frac{1}{3} \qquad \text{Eq. C5}$$

For this case $R^* = 2/3$.

The mean apparent co-plunge $\bar{\gamma}^*$ could be defined as:

$$\bar{\gamma}^* = \int_A \gamma^*\rho dA = \int_{\gamma^*=0}^{\gamma^*=\pi/2}\int_{\alpha^*=0}^{\alpha^*=2\pi}\left(\gamma^*\right)(\rho)\left(\sin\gamma^*\,d\alpha^*\,d\gamma^*\right)$$

$$\text{Eq. C6}$$

For a uniform distribution $\bar{\gamma}^*$ equals 1 radian, or $\sim57°$, and not 45° or $\cos^{-1}(R^*) = 60°$. The mean apparent co-plunge $\bar{\gamma}^*$ for a biased uniform distribution equals 45°, and not $\cos^{-1}(R^*) \approx 48°$.

For fracture orientation data obtained from a borehole, if $S^*>1/3$, or $R^*<2/3$, then the mean *in situ* co-plunge should exceed the 57° mean of a uniform distribution. If $S^*<1/3$, or $R^*>2/3$, then the mean *in situ* co-plunge should be less than the 57° mean of a uniform distribution.

Where fracture pole trends and plunges are chosen at random from the intervals 0°–360° and 0°–90°, respectively, the value for ρ is given by Equation B7. Solving Equation C3 for this case yields:

$$S^* = 1 - \frac{2}{\pi} \approx 0.363 \qquad \text{Eq. C7}$$

with $R^* = 2/\pi \approx 0.637$.

APPENDIX D
PRINCIPAL MOMENTS OF INERTIA

For points on a surface, the moment of inertia about a particular axis is defined by the following equation:

$$I = \int_A \rho dA\, d^2 \qquad \text{Eq. D1}$$

where ρ is the pole density within incremental element of area dA, and d is the distance from dA to the axis of rotation. The integral is over the surface of the object in question, which here is a lower hemisphere. Recasting (D1) in terms of α and γ:

$$I = \int_{\gamma^* = 0}^{\gamma^* = \pi/2} \int_{\alpha^* = 0}^{\alpha^* = \pi/2} \rho \sin\gamma^* \, d\alpha^* d\gamma^* d^2$$

Eq. D2

A continuous biased uniform pole distribution on a unit lower hemisphere is axially symmetric about a vertical axis, which is the z-axis here. The moment of inertia about the z-axis is termed I_z. The x- and y-axes lie in a horizontal plane that divides the lower hemisphere from the upper hemisphere. Given the axial symmetry of the distribution, the moments of inertia about these two axes are equal (i.e. $I_x = I_y$).

To find I_z, $\rho = \cos\gamma/\pi$, and $d = \sin\gamma$. Substituting these values into Equation D2 yields:

$$I_z = \frac{1}{2}$$

Eq. D3

For the moment about a horizontal axis, consider the y-axis. As above, $\rho = \cos\gamma/\pi$, and $dA = (\sin\gamma) \, d\gamma d\alpha$, but $d = [(\sin\gamma \cos\alpha)^2 + (\cos\gamma)^2]^{1/2}$. Substituting these values into Equation D1 yields:

$$I_y = \frac{3}{4}$$

Eq. D4

Comparing Equations D3 and D4 reveals the principal moments are related as follows for a biased uniform distribution:

$$I_y = I_x = \frac{3}{2} I_z$$

Eq. D5

For a perfect girdle distribution about a vertical axis, the poles will lie in a horizontal plane and will intersect a lower hemisphere along a great circle of unit radius. The expression for the moment differs from that of Equation D1:

$$I = \int_{\alpha = 0}^{\alpha = 2\pi} \rho r d\alpha \, d^2$$

Eq. D6

where $r = 1$ and the pole density ρ is measured around the girdle circle.

To find I_z for an axially symmetric girdle distribution with a uniform density, set $\rho = 1/(2\pi)$, the reciprocal of the circle circumference, and $d = 1$. Substituting these values for ρ and d into Equation D6 yields:

$$I_z = 1$$

Eq. D7

For the moment about the y-axis, $d = \cos\alpha$. Equation D6 yields:

$$I_y = \frac{1}{2}$$

Eq. D8

Again, given the axial symmetry of the distribution, $I_x = I_y$. The principal moments for a girdle distribution then are related as follows:

$$I_y = I_x = \frac{1}{2} I_z$$

Eq. D9

For the case where fracture pole trends and plunges are chosen at random from the intervals 0°–360° and 0°–90°, respectively, ρ is given by Equation B7. Moment I_z is found using $d = \sin\gamma$. Substituting these values into Equation D1 yields:

$$I_z = \frac{1}{2}$$

Eq. D10

For the moment about the y-axis, $d = [(\sin\gamma \cos\alpha)^2 + (\cos\gamma)^2]^{1/2}$. Substituting the appropriate values into Equation D1:

$$I_y = \frac{3}{4}$$

Eq. D11

Again, given the axial symmetry of the distribution, $I_x = I_y$.

APPENDIX E
BOUNDING ANGLES FOR BINS FOR CHI-SQUARE ANALYSES

Bin rings are defined here such that the total probability of a pole being in a given ring is the same for each of the N rings into which the lower hemisphere is divided:

$$\int_A \rho dA = \frac{1}{N}$$

Eq. E1

where the area of integration is the area of the "edge" of the ith ring. The ith ring is bounded below by and above by angles γ^*_{i-1} and γ^*_i, respectively, where the angles are measured with respect to the borehole (see Figure 2).

For a uniform distribution ρ equals $1/2\pi$. Recasting Equation E1 in terms of angles α^* and γ^*, and substituting Equation A11 for dA and $1/2\pi$ for ρ:

$$\int_{\gamma^*_{i-1}}^{\gamma^*_i} \int_0^{2\pi} \frac{1}{2\pi} \sin\gamma^* \, d\alpha^* d\gamma^* = \frac{1}{N}$$

Eq. E2

Solution of Equation E2 yields:

$$\gamma^*_i = \cos^{-1}\left(\cos\gamma^*_{i-1} - \frac{1}{N}\right)$$

Eq. E3

Examining the first few terms of $\gamma*_i$ reveals a simple iterative pattern:

$$\gamma*_i = \cos^{-1}\left(1 - \frac{i}{N}\right) \qquad \text{Eq. E4}$$

For a biased distribution $\rho = (1/\pi)\cos\gamma*$ and Equation E1 becomes:

$$\int_{\gamma*_{i=1}}^{\gamma*_i} \int_0^{2\pi} \left(\frac{\cos\gamma*}{\pi}\right)\left(\sin\gamma* d\alpha* d\gamma*\right) = \frac{1}{N} \qquad \text{Eq. E5}$$

Solving for $\gamma*_i$:

$$\gamma*_i = \sin^{-1}\left[\left(\sin^2\gamma*_{i-1} + \frac{1}{N}\right)^{1/2}\right] \qquad \text{Eq. E6}$$

The first few terms of $\gamma*_i$ again reveal a simple iterative pattern:

$$\gamma*_i = \sin^{-1}\{[i/N]^{1/2}\} \qquad \text{Eq. E7}$$

Where fracture pole trends and plunges are selected at random, $\rho = (1/\pi^2 \sin\gamma*)$. Substituting this value of ρ into Equation E1 yields:

$$\gamma*_i = \frac{\pi}{2N} + \gamma*_{i-1} \qquad \text{Eq. E8}$$

The angle $\Delta\gamma* = \gamma*_i - \gamma*_{i-1}$ defining the rings widths is a constant. Equation E8 reduces to the following expression:

$$\gamma*_i = i(2\pi/N) \qquad \text{Eq. E9}$$

Equations E4 and E7 yield simple expressions for bin ring radii. Let the radius of the equal area diagram be r. The relationship between the radial distance r_i

on an equal area diagram and angle $\gamma*_i$ is (see Figure 2B):

$$r_i = \sqrt{2}r \sin\frac{\gamma*_i}{2} \qquad \text{Eq. E10}$$

Using the half-angle relation:

$$\sin\frac{\gamma*}{2} = \sqrt{\frac{1}{2}\left(1 - \cos\gamma*\right)} \qquad \text{Eq. E11}$$

Equation E10 yields:

$$r_i = r\sqrt{1 - \cos\gamma*_i} \qquad \text{Eq. E12}$$

Substituting the expression for $\gamma*_i$ in Equation E4 into Equation E12 gives the radii for bin rings for a uniform distribution:

$$r_i = r\sqrt{1 - \left(1 - \frac{i}{N}\right)} = r\sqrt{\frac{i}{N}} \qquad \text{Eq. E13}$$

To find the bin radii for a biased uniform distribution, Equation E12 is recast:

$$r_i = r\sqrt{1 - \sqrt{1 - \sin^2\gamma*_i}} \qquad \text{Eq. E14}$$

Substituting the expression for $\gamma*_i$ in Equation E7 into Equation E14 gives the radii for bin rings for a biased uniform distribution:

$$r_i = r\sqrt{1 - \sqrt{1 - \frac{i}{N}}} \qquad \text{Eq. E15}$$

Examples of bin rings segregating fracture pole distributions representing uniform and biased uniform distributions are shown in Figure 6.